

Fabricated CeO₂ nanopowders as a novel sensing platform for advanced forensic, electrochemical and photocatalytic applications

B. S. Rohini¹ · H. Nagabhushana¹ · G. P. Darshan² · R. B. Basavaraj¹ · S. C. Sharma^{3,4} · R. Sudarmani⁵

Received: 17 August 2017 / Accepted: 26 September 2017 / Published online: 25 October 2017
© The Author(s) 2017. This article is an open access publication

Abstract In Forensic investigation, identification of various types of ridge details are essential in order to fix the criminals associated in various crimes. Even though several methods and labeling agents are available to visualize latent finger prints (LFPs) there is still simple, accurate, cost-effective, and non-destructive tool is required. In the present work, CeO₂ nanopowders (NPs) are prepared via simple solution combustion route using *Tamarindus indica* fruit extract as a fuel. The optimized NPs are utilized for visualization of LFPs on various surfaces by powder dusting method. Results revealed that visualized LFPs exhibit Level 3 features such as pores and ridge contours under normal light with high sensitivity and without background hindrance. The photometric characteristics of the prepared samples exhibit blue color emission and highly useful in warm light emitting diodes. The photocatalytic studies were carried out with different Methylene blue (MB) dye concentration and pH values. The obtained results reveal that the CeO₂ NPs exhibits an excellent

photocatalytic properties which can act as a good catalytic reagent. The findings demonstrate that the prepared NPs are quite useful as a labeling agent for visualization of LFPs, efficient catalysts for dye degradation as well as solid-state lighting applications.

Keywords *Tamarindus indica* · Latent fingerprints · Solution combustion route · Photoluminescence · Photocatalytic activity

Introduction

Fingerprints (FPs) have provided a vital source of forensic evidence for human identification and individualization. The patterns on the FPs are individual to each person and remain same throughout lifespan. Normally most of FPs seen in the daily life is latent and invisible to naked eyes; as a result, some certain methods are necessary to recognize personal identification in forensic science. Till date numerous methods (chemical, optical) have been established to recognize LFPs. However, the recognition was restricted only level 1 and level 2 ridge details due to the poor image qualities (Saif et al. 2015; Sharma et al. 2014; Wang et al. 2015a, b, c).

Further, the level 1 and 2 features are easily forged, by the generation and use of artificial skin imprints. However, the analysis of level 3 features required some efficient nano powders with uniform particle size and morphology (Basavaraj et al. 2017; Dhanalakshmi et al. 2017; Venkatachalaiah et al. 2017). Hence, there is an urgent need to progress a simple and efficient route in developing LFPs with superior sensitivity, little background, extraordinary efficiency, lesser toxicity and stress-free detection of LFPs, which is the essential requirement for forensic

✉ G. P. Darshan
darshubavimane@gmail.com

¹ Prof. C.N.R. Rao Centre for Advanced Materials Research, Tumkur University, Tumkur 572 103, India
² Department of Physics, Acharya Institute of Graduate Studies, Bangalore 560 107, India
³ Avinashilingam Institute for Home Science and Higher Education for Women University, Coimbatore 641 043, India
⁴ Department of Mechanical Engineering, Jain Group of Institutions, Jain University, Bangalore 560 069, India
⁵ Department of Electronics and Communication, Avinashilingam Institute for Home Science and Higher Education for Women University, Coimbatore 641 043, India

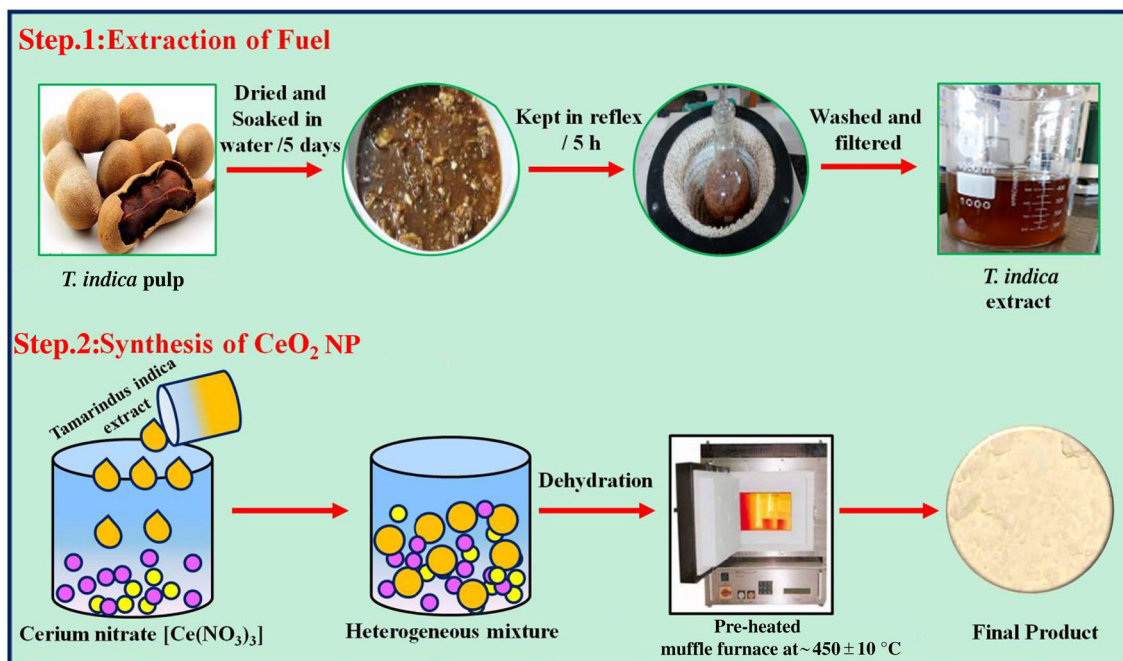


Fig. 1 Schematic representation to show various steps involved in extraction of fuel and synthesis of CeO₂ NPs by solution combustion route

investigators. Further, most of the available literature for the detection of LFPs is due to excited ultraviolet (UV) radiation; rare earth doped fluorescent nanopowders can enhance FPs contrast. Conversely, UV light has many drawbacks including high background interference owing to the significant auto-fluorescence from the substrates, photo damage to the skin and eyes of the operators, and the possibility of severe irradiation-induced damage. Therefore, NPs are highly essential for the recognition of level 3 ridge details under normal light in the field of forensic science (Darshan et al. 2016; Suresh et al. 2017).

In recent years, the change in physiochemical properties of bulk material to corresponding nano regime has created numerous interest for material scientists. Due to its versatile applications in gas sensors, fuel cells, solar cells and very good photocatalytic activity, Cerium oxide nanoparticles have attracted much attention in recent years (Choi et al. 2006; Lehnen et al. 2014; Liu et al. 2013; Sathyamurthy et al. 2005; Sun et al. 2005). Its diverse applications is due to the efficiency of transfer of elevated oxygen from reduced to oxidized state (Lin et al. 2013; Zhou and Rahaman 1997). Till date, various reports of CeO₂ synthesis routes are available in the literatures. In the recent years, bio-synthesis route using plant extracts is found to be environmental friendly, novel and inexpensive. Further, it does not require high pressure and high temperature (Derakhshandeh and Soleimannejad 2016; Huang et al. 2005; Maensiri et al. 2014; Maensiri et al. 2007; Wang et al. 2010). With no *f* electron CeO₂ would be a good

host material for photoluminescent materials (Jamshidi et al. 2013; Weber 1973). Ling Li et al. reported violet/blue emission of cerium composited with silicon for its good compatibility with the silicon-based materials used in the fabrication of optoelectronics devices (Li et al. 2015; Arumugam et al. 2015; Ketzial and Nesaraj 2011; Malle-shappa et al. 2015; Lee et al. 2014; Lopez and Mendoza 2013).

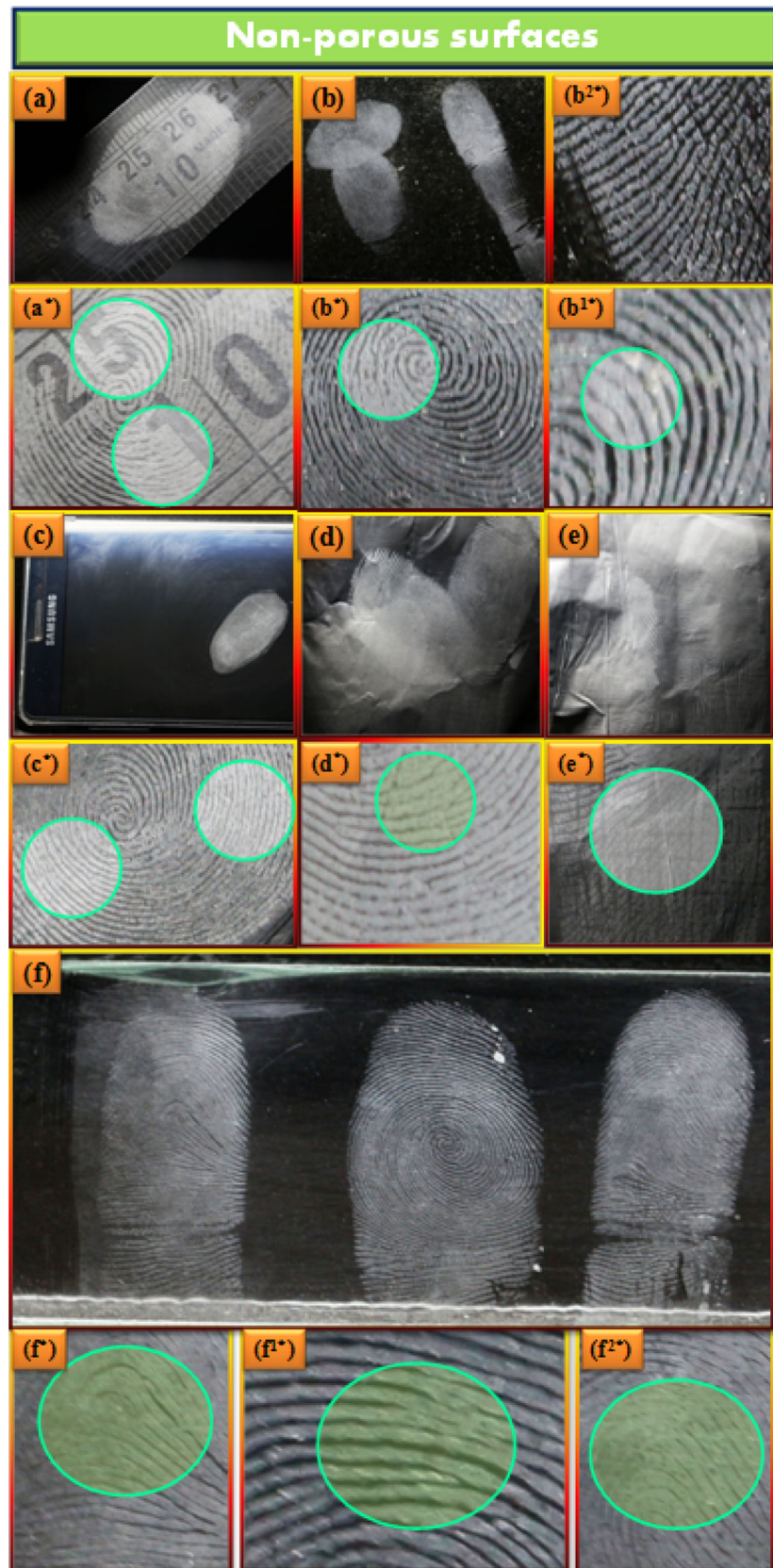
Till date, limited reports are available for the synthesis of CeO₂ NPs by solution combustion method using *Tamarindus indica* fruit extract as fuel. Further, the optimized product is utilized for visualization of LFPs on both porous and non-porous surfaces. Finally, the photocatalytic degradation is examined using MB as a dye. The detailed investigation on the mechanism related to the photocatalytic degradation is discussed.

Experimental

Fruit extract

Tamarindus indica fruit is collected from the local market of Tumkur and dried for about 5 days under the sunlight. 100 g of *T. indica* fruit was soaked in water for ~ 16 h. The obtained solution is kept in reflux for ~ 5 h and then washed several times with distilled water and filtered. Finally, the obtained *T. indica* fruit extract was stored in refrigerator until further use.

Fig. 2 a–f LFPs visualized by staining calcined CeO_2 (15 ml) NPs on various non-porous surfaces and (a*, b*, b^{1*}, b^{2*}, c*, d*, e* and f^{1*}, f^{2*}) shows the enlarged views of FPs which exhibits various ridge prints



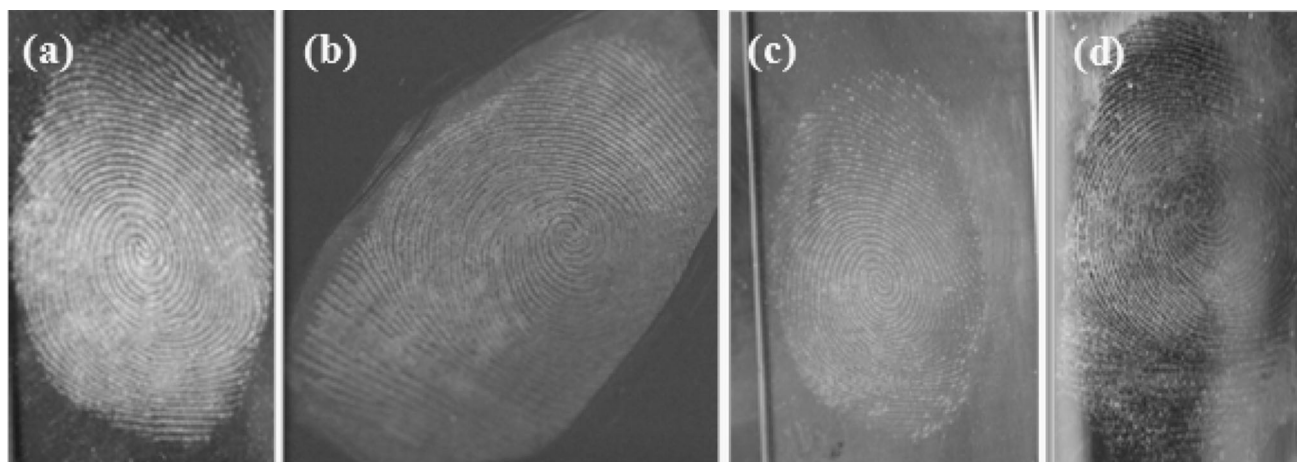
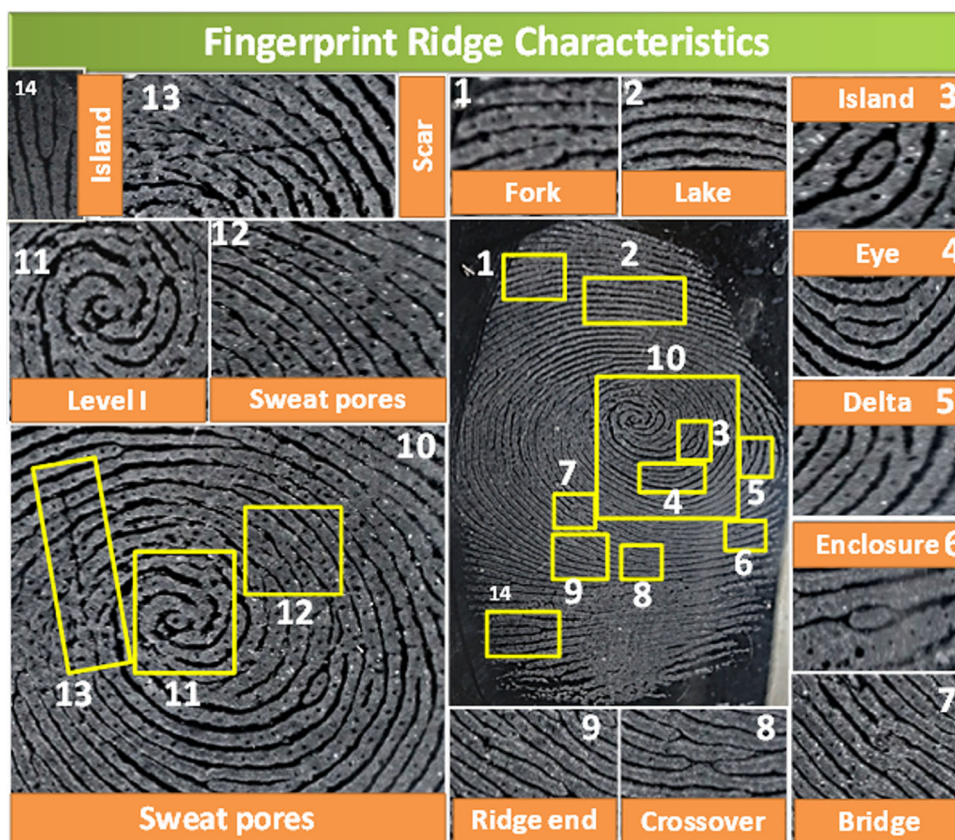


Fig. 3 LFPs aged on the surface of glass for various periods of time, stained by calcined CeO_2 (15 ml) NPs under normal light **a** 1 day, **b** 1 week, **c** 2 weeks and **d** 3 weeks

Fig. 4 Various ridge levels of FP patterns visualized by staining optimized calcined CeO_2 (15 ml) NP on glass surface under normal light



Synthesis

A simple solution combustion route is used to prepare pure CeO_2 NPs using *T. indica* fruit extract as fuel. Initially, Cerium (III) nitrate $[(\text{Ce}(\text{NO}_3)_3 \cdot 6\text{H}_2\text{O})]$: 0.5 g) is taken in a petri dish and 5 ml of *T. indica* fuel is added (1 g of extract is dissolved in 250 ml of water and stirred for 10 min). The

precursor solution is stirred thoroughly using magnetic stirrer (~ 5 – 10 min) till homogeneous mixture is obtained. The resultant reaction mixture is placed in a preheated muffle furnace maintained at a temperature of $\sim 450 \pm 10$ °C. The mixture undergoes dehydration with liberation of large amount of gases. Finally, a product is left behind in the petri dish. The portion of obtained

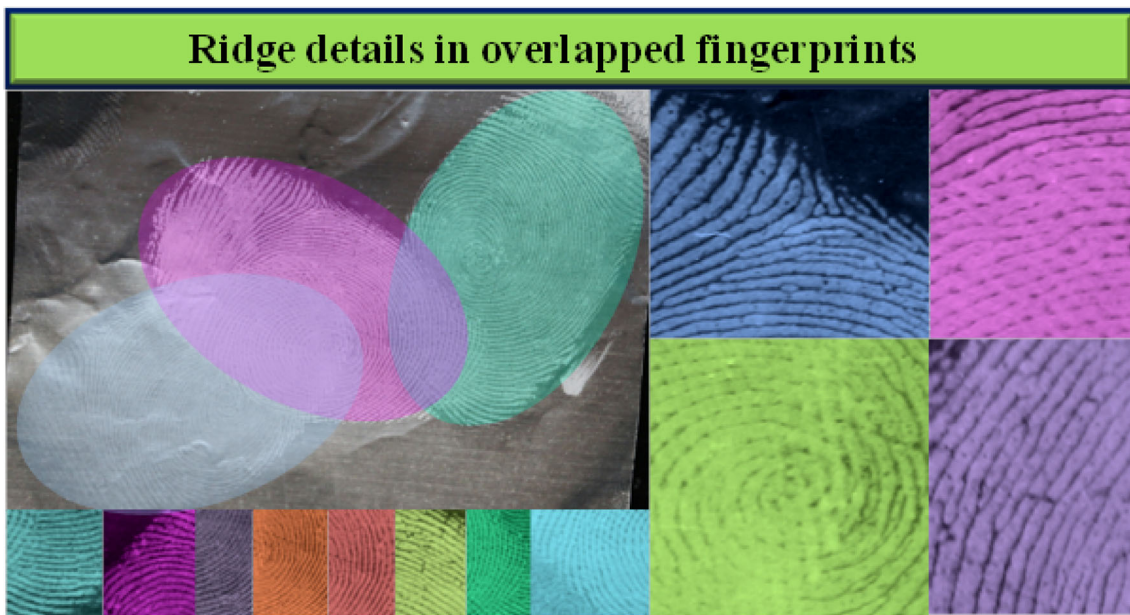


Fig. 5 Overlapped and various ridge details of FP patterns visualized using calcined CeO_2 (15 ml) NP on aluminium foil surface

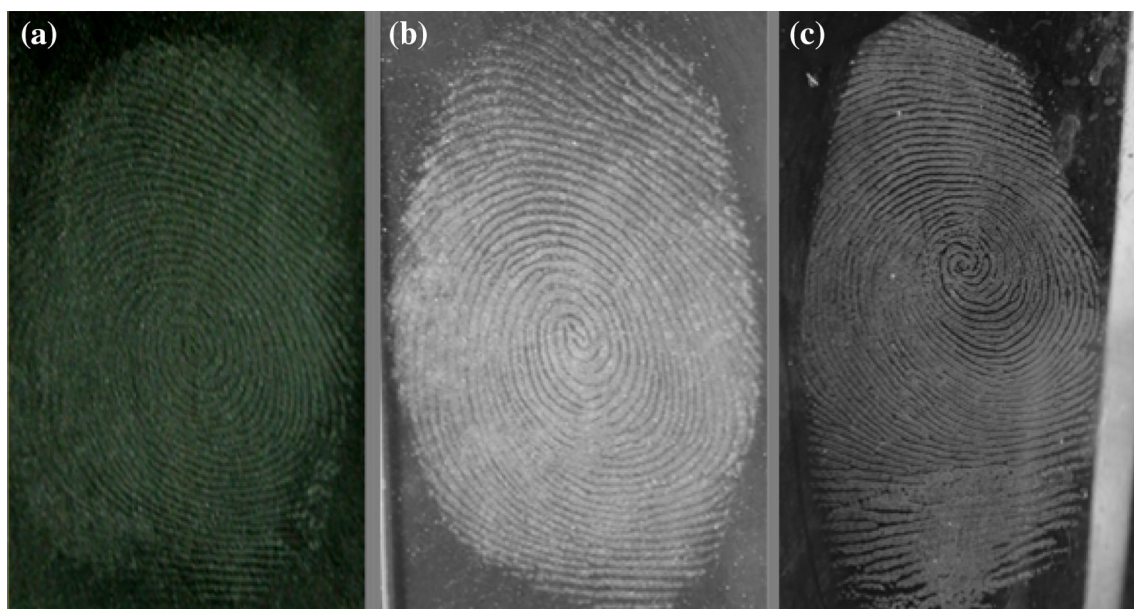


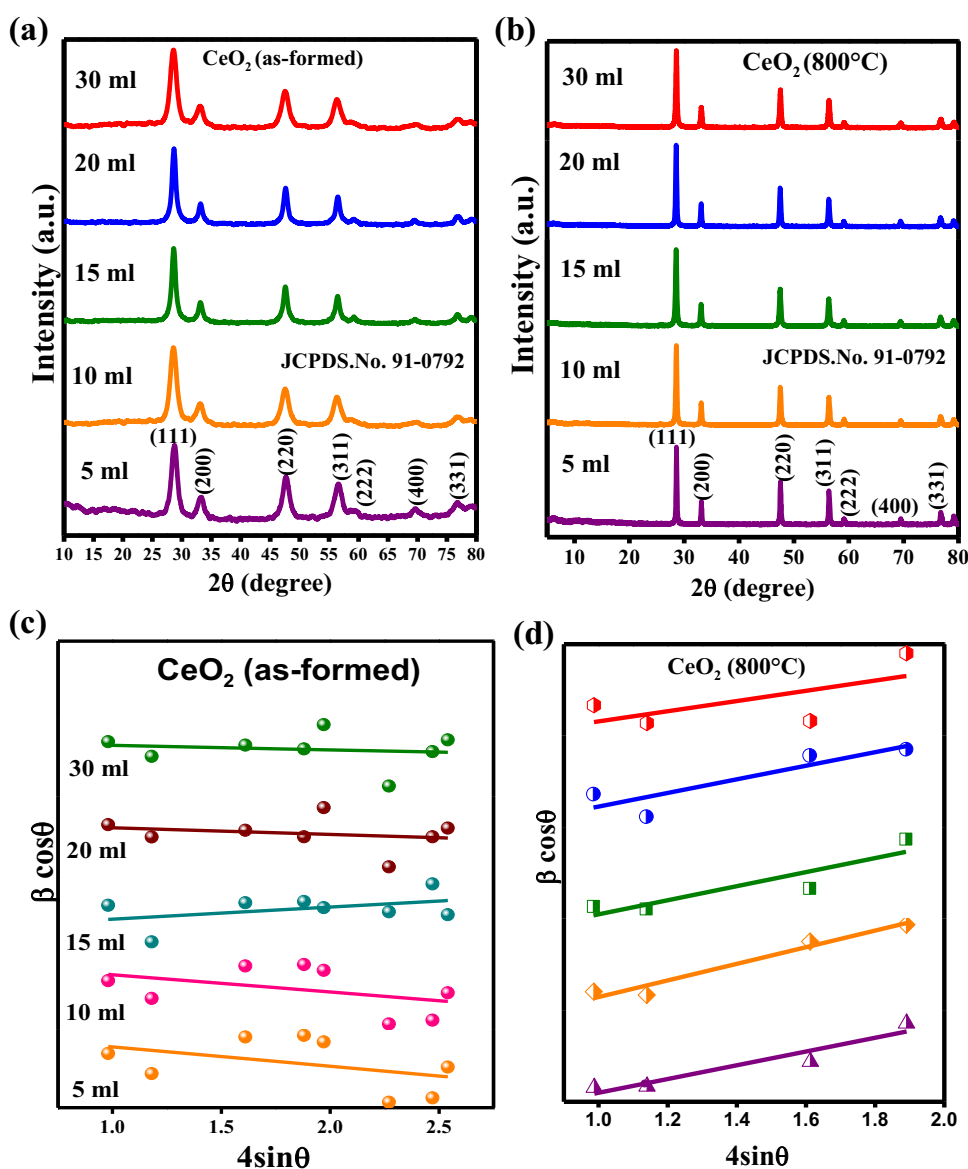
Fig. 6 Comparison of FP images visualized by staining Fe_2O_3 , TiO_2 and calcined CeO_2 (15 ml) NP on glass surface under visible light

product is calcined at $\sim 800^\circ\text{C}$ for 3 h. The same experimental procedure is repeated for different concentrations of *T. indica* extract (5, 10, 15, 20 and 30 ml). The prepared as-formed and calcined CeO_2 NPs were used for further characterization. Figure 1 shows the schematic representation of the steps involved for the extraction of *T. indica* fuel and synthesis of CeO_2 NPs.

Characterization

The powder X-ray diffraction (PXRD) measurements were performed on the Shimadzu made X-ray diffractometer (Shimadzu 7000) with graphite monochromatized Cu-K_α radiation ($\lambda = 0.15406\text{ nm}$) to study the phase and purity of the prepared samples. The surface morphology is studied

Fig. 7 PXRD patterns and W–H plots of CeO₂ NPs (**a, c**) as-formed and (**b, d**) calcined at 800 °C



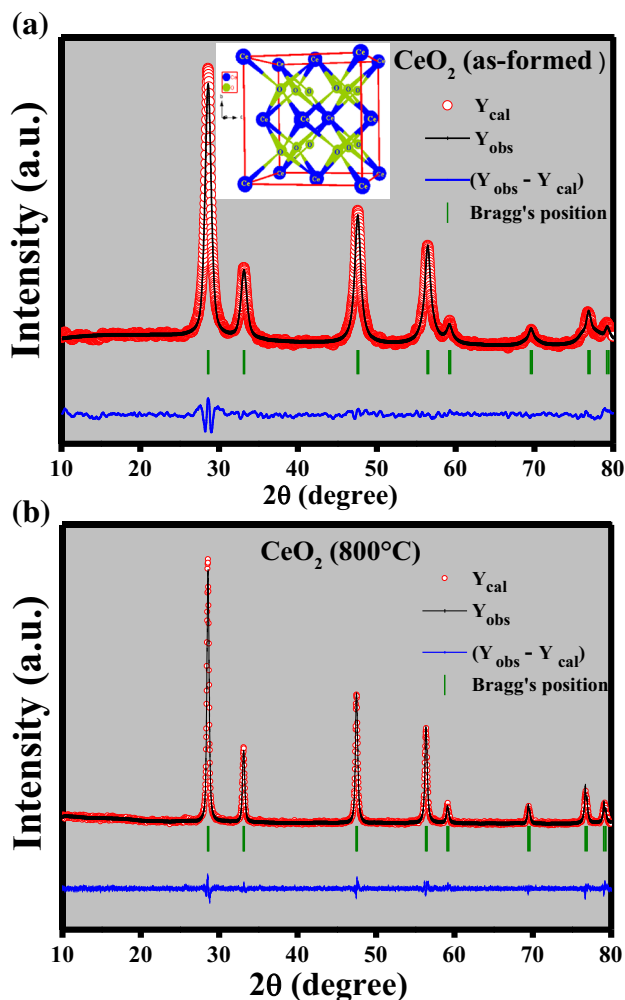
by Hitachi made table top scanning electron microscope (SEM) (Hitachi-TM 3000). Transmission electron microscope (TEM) (Hitachi H-8100, Kevex sigma TM Quasar, USA) is used to estimate the crystallite size of the material. Spectrophotometer (Lambda-35, Perkin Elmer) is used to study the diffuse reflectance of the prepared material. Spectrofluorimeter equipped with Fluorolog-3 (Jobin–Yvon) is utilized to measure the photoluminescence (PL) properties. The Fourier transform infrared (FTIR) spectrum is recorded in Bruker alpha made FTIR instrument. The Jobin–YVON Horiba LABRAM-HR-Visible micro Raman system is used for Raman studies with He–Ne laser (~ 632.8 nm) as the source.

Visualization of LFPs using CeO₂ NPs as labeling agents

The LFPs are collected from healthy donor on various surfaces including porous and non-porous surfaces. The hands of the donor are washed thoroughly with soap and dried before impression. Subsequently, the washed fingers are gently pressed against various porous and non-porous surfaces to acquire LFPs. Thereafter, the obtained LFPs are stained by optimized CeO₂ (15 ml) NP using soft feature brush with smooth powder brushing method. Finally, developed FPs are visualized under normal light using a Nikon D3100/AF-S Nikkor 50 mm f/2.8G ED lens digital camera.

Table 1 Estimated average crystallite size, strain, and energy gap (E_g) values of the as-formed and calcined CeO₂ NP

Sample	Fuel conc. (ml)	Crystallite size (nm)		Strain X 10 ⁻³	Energy gap (E_g) eV
		Scherrer's method	W-H plots		
As-formed	5	7	15	11	3.24
	10	5	7	10	3.60
	15	5	6	3	3.45
	20	6	8	3	3.38
	30	5	6	3	3.69
800 °C	5	41	18	71	2.86
	10	39	18	29	3.16
	15	71	44	26	3.19
	20	81	45	36	3.20
	30	45	31	22	2.86

**Fig. 8** Rietveld refinement of **a** as-formed and **b** calcined CeO₂ NPs (800 °C) (Inset: Packing diagram)

Results and discussion

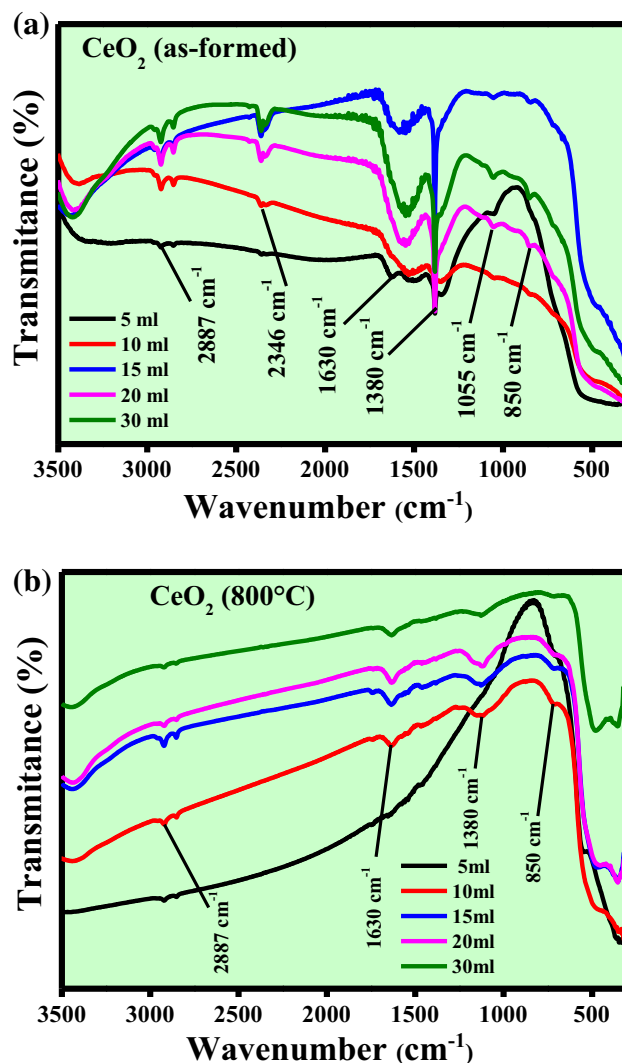
In order to inspect its suitability for recognizing latent fingerprints (LFPs), optimized CeO₂ NPs were stained on the LFPs developed on various non-porous substrates, namely stainless steel, glass, mobile screen and aluminium foil. In the present studies, all FPs were extracted from the same donor. Figure 2 display the LFPs images visualized by staining CeO₂ NPs illuminated under normal white light. A complete ridge details including type 1, 2 and 3 patterns with good adhesion, well-defined ridge flow and ridge orientation field is observed. Further, the FPs were well defined in terms of finger ridge details which due to their nano-sized CeO₂. FP types have been described into three groups; (i) level 1 features are described by fingerprint ridge flow and general morphological information, (ii) level 2 features provide pattern matching followed detection of individual fingerprint ridges, (iii) level 3 features is defined as all attributes of a ridge, including shape, width, pores and curvature. Further, the stability of the prepared powders are assessed by aging the FPs up to 21 days and displayed comparable brightness (Fig. 3). The brightness of the CeO₂ NPs-stained LFPs specifies that the NPs are physically and chemically steady in ambient conditions. Figure 4 displays detailed ridge patterns (type 1, 2 and 3) developed on glass which consists of clear and distinct ridges of FPs can be undoubtedly detected under normal visible light. The level 2 details, such as the ridge bifurcation, island, scar, eye, bridge, ridge end, termination, lake and sweat pores, were clearly distinguished. Further, overlapped LFPs can be recognized on aluminium foil surfaces and shown in Fig. 5. The images clearly evident that the recognition of various ridge features includes level

Table 2 Structural parameters of CeO₂ NPs estimated using Rietveld refinement

Sample	Unit cell parameters		Atomic positions						Agreement values	
	Atom	x	y	Z	Biso	Occ				
CeO ₂ as-formed	Fm-3m (No. 225) (body centered cubic)	$a = b = c = 5.4049 \text{ \AA}$,	0.000	0.000	0.000	0.000	0.684	$\chi = 0.1467$, $R_p = 2.53$,		
		$V = 157.89 \text{ \AA}^3$, density = 7.039 g cm^{-3}	0.25	0.25	0.25	0.25	1.164	$R_{exp} = 8.42$, GOF = 0.39		
CeO ₂ calcined at 800 °C	Fm-3m (No. 225) (body centered cubic)	$a = b = c = 5.411 \text{ \AA}$,	0.000	0.000	0	0	0.558	$\chi = 1.46$, $R_p = 7.25$,		
		$V = 158.54 \text{ \AA}^3$, density = 7.082 g cm^{-3}	0.25	0.25	0.25	0.25	1.000	$R_{exp} = 8.15$, GOF = 1.2		

1, level 2 and also level 3 identification. Further, LFPs developed on glass were compared with commercially available (Fe₂O₃ and TiO₂) powders and shown in Fig. 6. According to the detailed results obtained in the present study, we can observe the FP types specifically ridge flow, sweat pore, terminates, bifurcation and lack corresponding to the levels 1–3. Therefore, it is authorized that the probability for the recognition of the foremost ridge details of FPs in different surfaces was well established by optimized CeO₂ NPs. The high-quality FP images developed on non-porous surfaces display the possible usage of CeO₂ NPs fabricated via green synthesis route for forensic application.

Figure 7a, b shows the PXRD patterns of as-formed and calcined (800 °C) CeO₂ NPs. All the diffraction patterns are well indexed to JCPDS card No. 81-0792 (Mallehappa

**Fig. 9** FTIR spectra of **a** as-formed and **b** calcined CeO₂ (5–30 ml) NPs

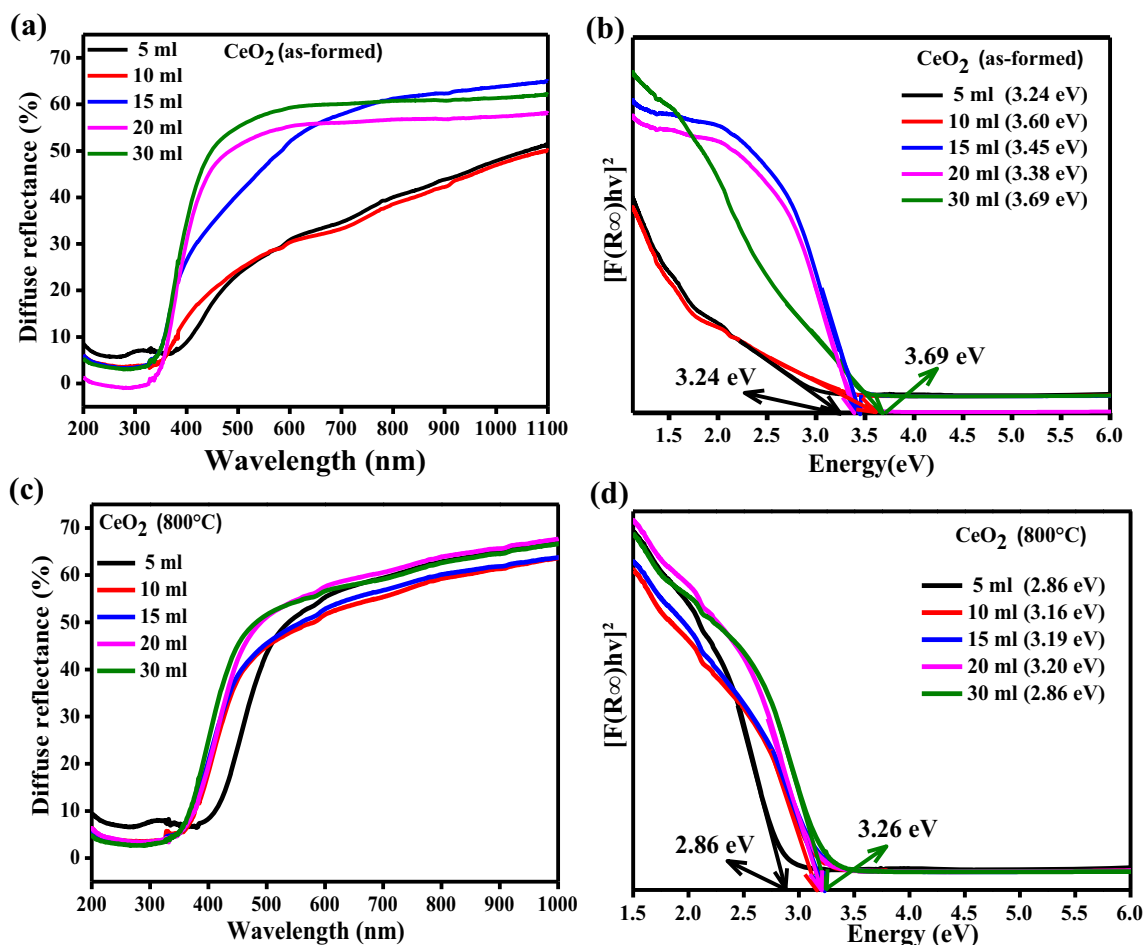


Fig. 10 a, c Diffuse reflectance spectra and b, d energy band gap plots of as-formed and calcined CeO₂ NPs

et al. 2014). The observed XRD peaks are well matched with the cubic planes (111), (200), (220), (311), (222), (400) and (311). No secondary or impurity peaks were present in the samples, which confirms the single cubic phase of CeO₂. However a small lower angle (28.51°) peak shift in the plane (111) is observed due to compressive stress. The average crystallite size (D) is estimated using Scherrer's relation:

$$D = \frac{k\lambda}{\beta \cos \theta}, \quad (1)$$

where λ is the wavelength of the X-ray radiation (1.54 Å), K is the constant (0.9), β is the full-width at half-maximum (FWHM), and θ is the diffracting angle. The estimated values of D are tabulated in Table 1. The lattice strain present in the product is estimated using the Williamson and Hall (W–H) plots using the following relation:

$$\beta \cos \theta = \frac{k\lambda}{D} + 4\varepsilon \sin \theta, \quad (2)$$

where λ is the wavelength of X-rays (1.54 Å), β is the full width at half maximum (in radians), θ is the diffraction angle, k is the shape factor (0.9), D is the crystallite size, and ε is the micro-strain. The plots of $\beta \cos \theta$ v/s $4 \sin \theta$ are shown in Fig. 7c, d. The slope of line gives the strain (ε) and intercept ($k \lambda / D$) on Y axis gives crystallite size. The estimated values of D and lattice strain present in the samples are listed in Table 1.

One of the drawbacks of the diffraction patterns is accurate determination of crystal structure because of the overlapping of the diffraction peaks. Therefore, Rietveld refinement analysis is used to create the virtual separation of the overlapped peaks (Fig. 8). The Rietveld refinement method is used to calculate the entire powder pattern of the sample with the different refinable parameters and to minimize the difference between the observed and calculated pattern by least square method. The lattice parameters are evaluated by performing Rietveld refinement using *FULLPROF* suit program (Konysheva et al. 2010;

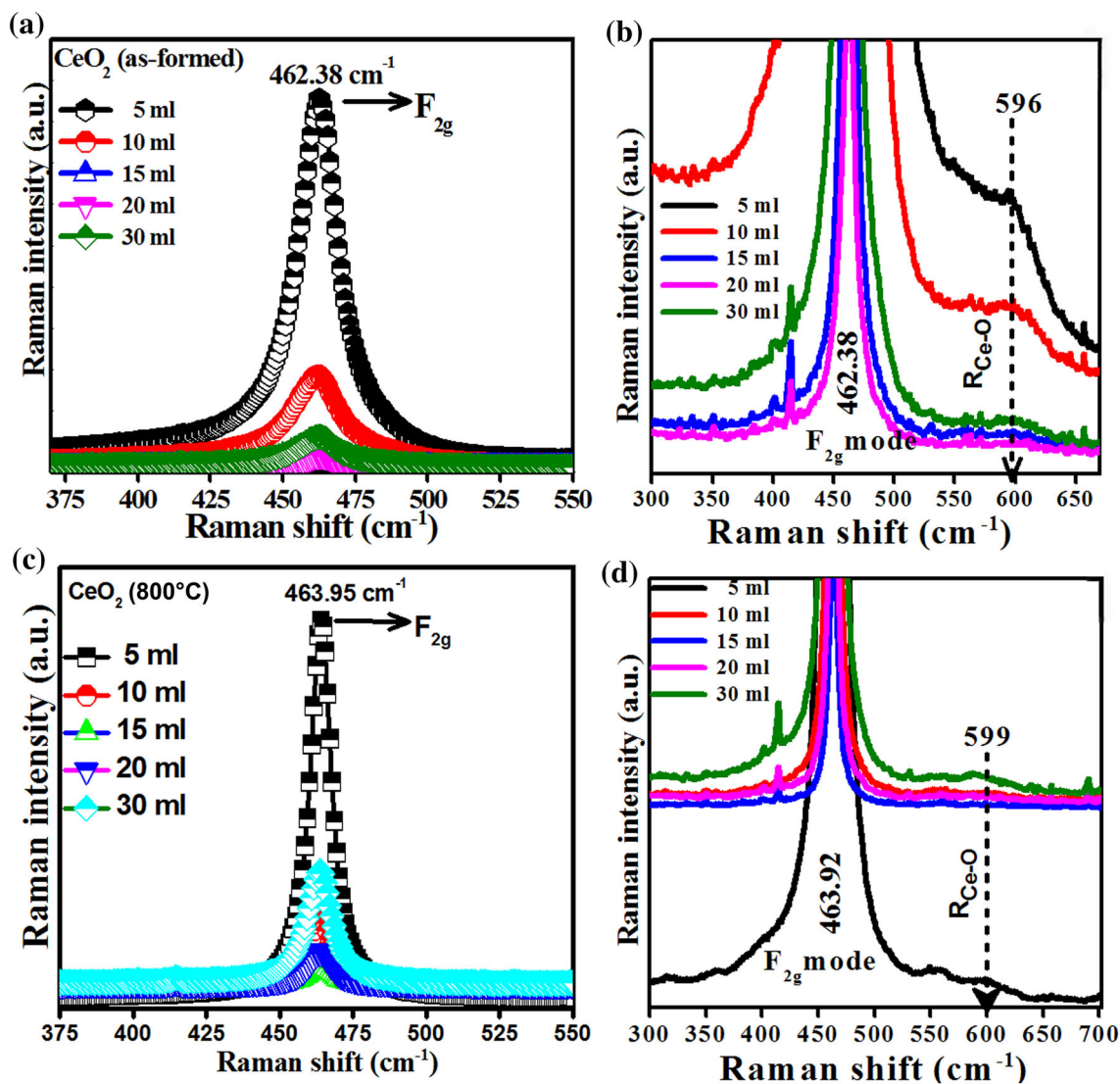


Fig. 11 a, c Raman spectra and b, d enlarged portion of Raman spectra of as-formed and calcined CeO₂ NPs

Table 3 Estimated Oxygen vacancies and crystallite size of CeO₂ NPs

CeO ₂	Conc. (ml)	463 Peak area	600 Peak area	Area _{Oxygen vacancies} /area _{F_{2g}} (%)	Crystallite size (Raman shift)
As-formed	5	3460740	5928.18	0.171	10.27
	10	966704.5	1874.74	0.194	7.78
	15	179867.2	2274.19	1.260	15.53
	20	110568.5	660.32	0.597	12.86
	30	303690.6	428.47	0.141	9.22
Calcined at 800 °C	5	1269350.0	9281.99	0.731	23.78
	10	278712.5	3776.97	1.360	22.62
	15	110219.9	917.794	0.833	20.95
	20	162636	2975.44	1.830	20.13
	30	554577.3	4039.91	0.728	19.07

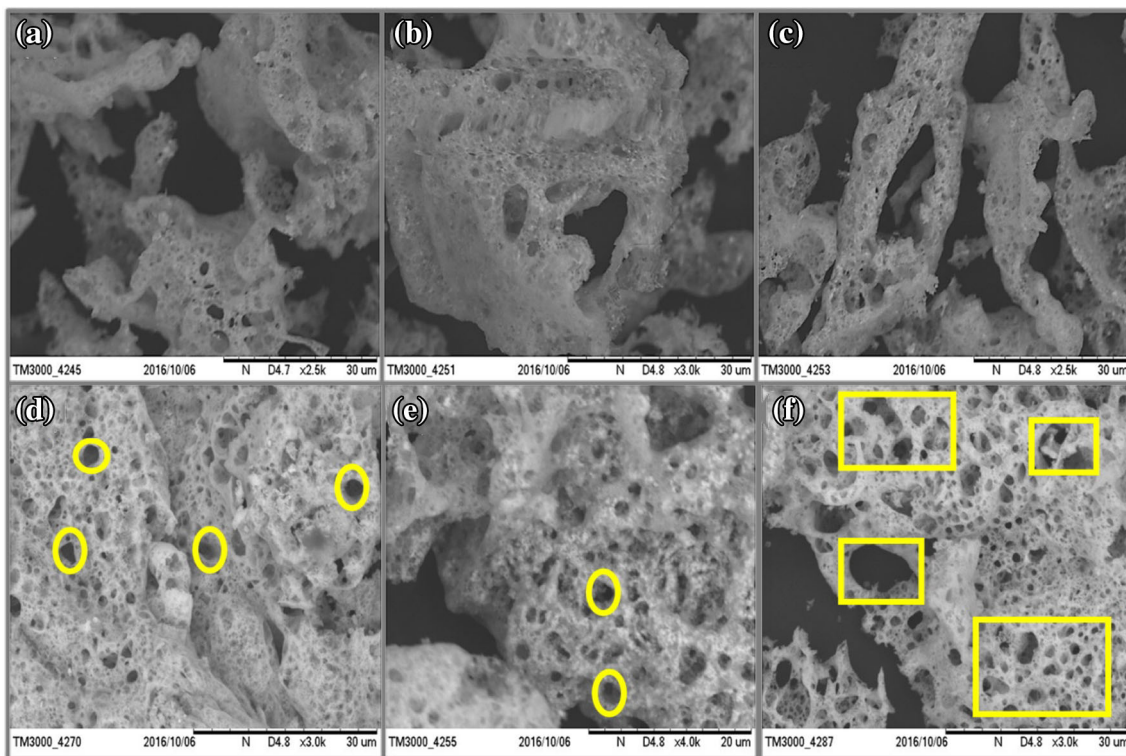


Fig. 12 SEM micrographs of **a–c** as-formed and **d–f** calcined (800 °C) CeO₂ (5, 15 and 30 ml) NPs

Mallesappa et al. 2016; Shivaram et al. 2014; Xiaoyuan et al. 2001).

Pseudo-Voigt function has been used to fit the several parameters like one scale factor, one zero shifting, six background, three cell parameters, five shape and width of the peaks, one global thermal factor and two asymmetric factors. The refined parameters namely occupancy, atomic functional positions for CeO₂ NPs are studied. The obtained results are in good agreement with the theoretically calculated ones. The space group used for the particular pattern is Fm-3m (No. 225). The refined parameters are tabulated in the Table 2. The obtained R_p , R_{wp} , R_{Braggs} , and χ^2 values indicate the good fit of the profile.

Figures 9a, b shows the FTIR spectra of the as-formed and calcined CeO₂ NPs prepared at different concentrations of *T. indica* extract (5–30 ml). From the figure, it is observed that the principal vibrational modes of CeO₂ NPs were in good agreement with the reported literature. In the calcined sample, a diffuse band observed at 2918 cm⁻¹ is due to the stretching vibration of the physically associated water (O–H) molecule. Another bending vibrational band of physically adsorbed water molecules is observed around 1619 cm⁻¹. A weak broad peak observed at 314 cm⁻¹ which is assigned to the Ce–O stretching band (Binet et al. 1994; Khan et al. 2013; Sahu and Rao 2000). The peak at

1350 cm⁻¹ is a characteristic vibration mode of CeO₂ (Ketzial and Nesaraj 2011; Yan and Zhu 2008).

The diffuse reflectance (DR) spectra of the as-formed and calcined samples of CeO₂ NPs are shown in Fig. 10a, c. The spectra are recorded in the range of 200–1100 nm wavelength at room temperature. It can be seen from the Fig. 10a, c that a strong absorption peak is observed in the range of 350–400 nm.

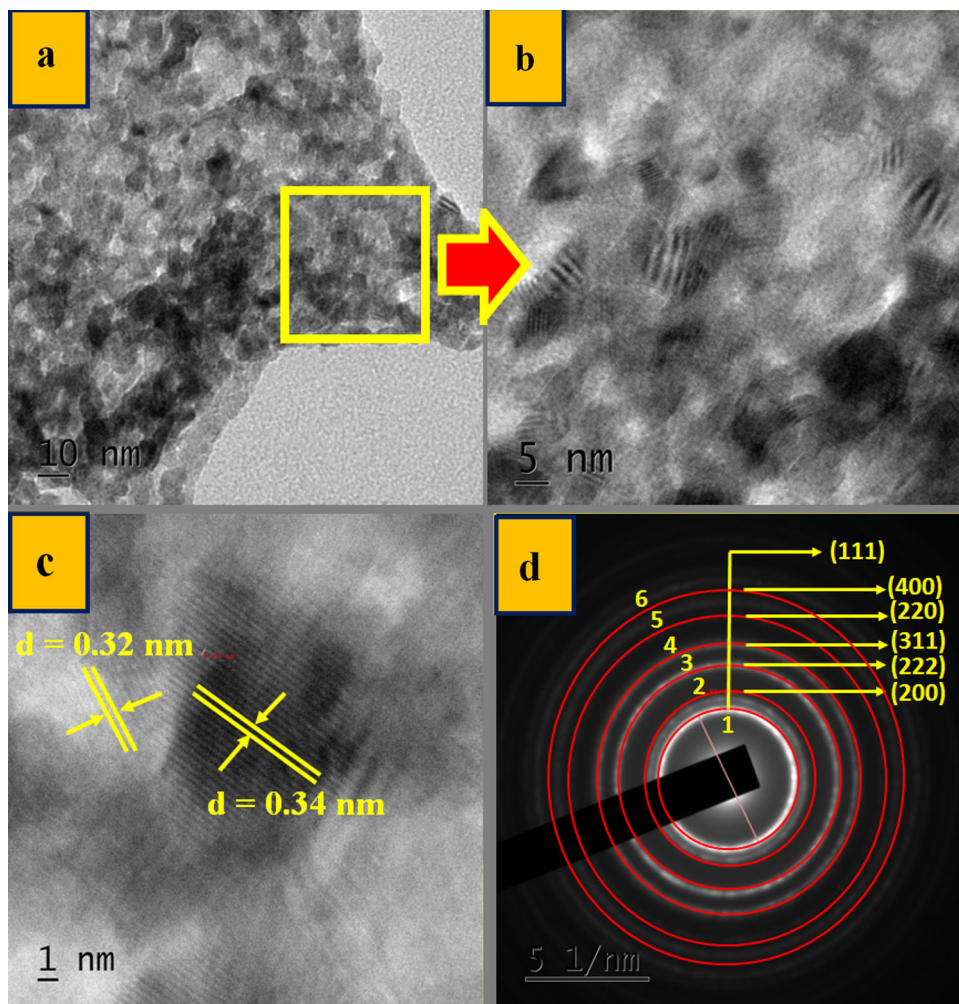
To determine the energy band gap, Kubelka–Munk function is used (Yuan et al. 2016). The Kubelka–Munk function $F(R_\infty)$ and band gap energy ($h\nu$) is estimated by utilizing the following equations:

$$F(R_\infty) = \frac{(1 - R_\infty)^2}{2R_\infty}, \quad (3)$$

$$h\nu = \frac{1240}{\lambda}, \quad (4)$$

where R_∞ is the reflection coefficient of the sample and λ is the absorption wavelength. The energy band gap values were evaluated and are summarized in Table 1. The energy band gap (E_g) values of as-formed CeO₂ NPs are found to be in the range of ~ 3.24–3.69 eV and that for calcined sample it was found to be ~ 2.86–3.20 eV, which is much lesser than the as-formed CeO₂ due to oxygen vacancies present in the sample (Fig. 10b, d), therefore, which gives

Fig. 13 **a** TEM, **b** enlarged view, **c** HRTEM image and **d** SAED pattern of as-formed CeO₂ (15 ml) NPs



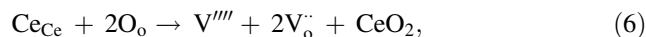
the evidence for the quantum confinement of calcined CeO₂ NPs. The decrease in E_g also indicate the red shift in the calcined sample (Table 1) (Li et al. 2015; Jorge et al. 2012; Periyat et al. 2011).

Figure 11a, c shows the Raman spectra of as—formed and calcined CeO₂ NPs and its enlarged portions are shown in Fig. 11b, d. The spectra exhibit four characteristic modes at ~ 254 , 460, 546 and 612 cm^{-1} (Balakrishnan et al. 2013). The mode at ~ 254 and 460 cm^{-1} are attributed to twice degenerated 2TA and first order F_{2g} , respectively. An F_{2g} mode confirms the fluorite cubic structure of the prepared samples and also signifies the symmetrical stretching vibration of the CeO₈ vibrational unit. A broad and asymmetric mode at ~ 460 cm^{-1} is red shifted as compared to bulk form owing to oxygen defects, phonon confinement, size distribution, deviation in phonon relaxation and strain present in the sample (Xu et al. 2017; Lopez et al. 2015). The other modes at ~ 546 and 612 cm^{-1} are due to oxygen vacancies (intrinsic and extrinsic). The relative intensities of Raman modes

at ~ 460 , 546 and 612 cm^{-1} are calculated based on the relation (Arumugam et al. 2015):

$$\frac{\text{Oxygen vacancies}}{F_{2g}} = \frac{(\text{Area}_{R_{\text{Ce-O}}})}{\text{Area } F_{2g}}. \quad (5)$$

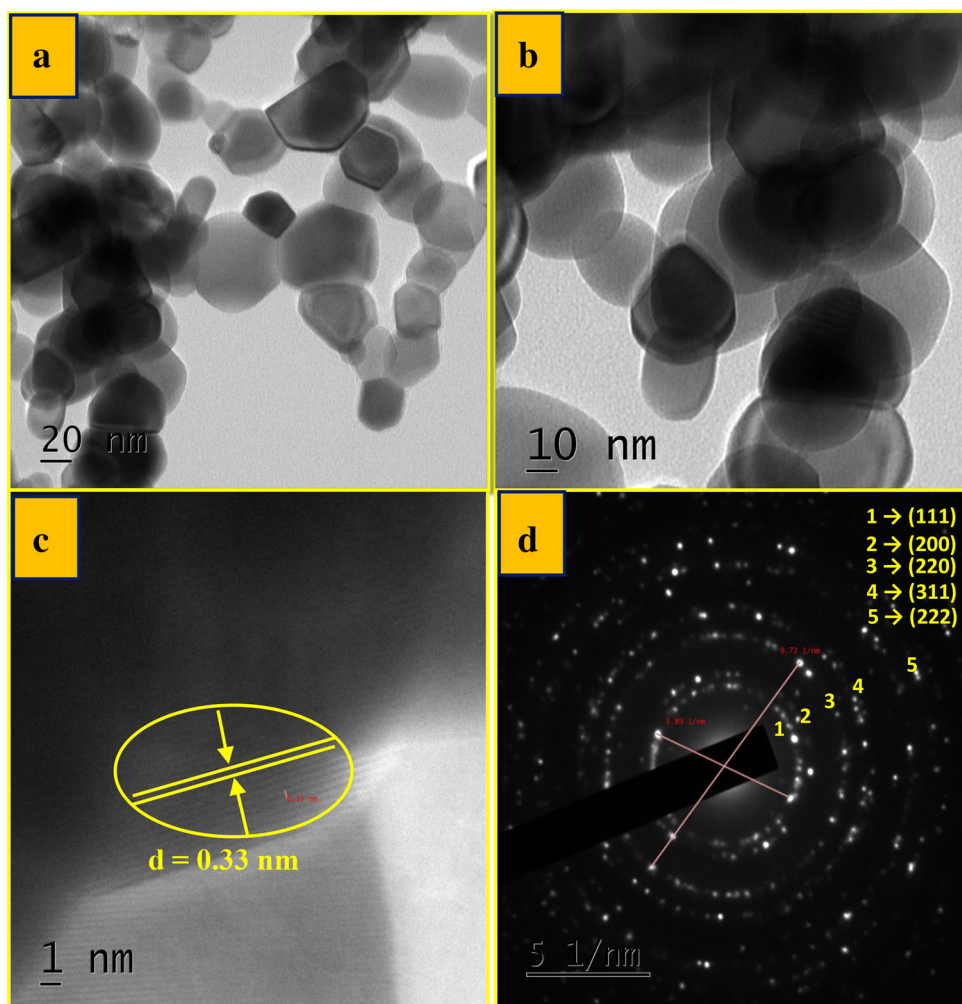
The rate of oxygen vacancies is estimated and given in Table 3. The probable reaction mechanism for intrinsic oxygen vacancies are:



Besides, the average crystallite size of the CeO₂ powder scale down to nano range leads to more oxygen loss (Jiang et al. 2012).

Figure 12 shows the SEM micrographs of as-formed and calcined CeO₂ NPs. It can be observed from the Fig. 12a–c

Fig. 14 **a, b** TEM, **c** HRTEM image and **d** SAED pattern of calcined CeO₂ (15 ml) NPs



that the particles are porous in nature. Particles are mostly containing voids with different sizes due to the evolution of large amount of gases during the combustion. The porosity and size of the voids increase with increase in temperature as observed in Fig. 12d–f. TEM, HRTEM images and SAED patterns of as-formed CeO₂ NPs are shown Fig. 13. The particles with agglomeration are observed in Fig. 13a. The estimated crystallite size varies between ~ 5 and 20 nm which is in good agreement with the PXRD results. The interplanar distance (d) was found to be around ~ 0.32 – 0.34 nm (Fig. 13c). The polycrystalline nature of the sample was further confirmed by SAED patterns. Figure 14 shows the TEM, HRTEM images and SAED patterns of calcined CeO₂ NPs. It is evident that in calcined samples the crystallinity has been increased as shown in Fig. 14a, b. The interplanar spacing d value is found to be ~ 0.33 nm.

Photoluminescence excitation spectrum of as-formed CeO₂ NPs upon 530 nm emission wavelength as shown in inset of Fig. 15a. The spectrum exhibit a sharp peak at \sim

386 nm. Figure 15a shows the PL emission spectra of as-formed CeO₂ NPs prepared with various fuel concentration under $\lambda_{\text{Exc}} = 386$ nm. The spectra exhibits peaks at ~ 362 , 391 and 441 nm may be attributed to surface defects, charge transition from the 4f band to the valence band of CeO₂ and oxygen vacancies (Li et al. 2008; Dang et al. 2010; Luo et al. 2015). The emission spectra of calcined CeO₂ NPs excited under 386 nm wavelength as shown in Fig. 15b, e. The spectra exhibits characteristic peaks at ~ 485 , 528 and 542 nm are believed to be due to surface defects and oxygen vacancies (Li et al. 2011; Arunkumar et al. 2014; Morshed et al. 1997; Maensiri et al. 2007).

The Commission Internationale de L'Eclairage (CIE) diagram of as-formed and calcined CeO₂ NPs is shown in Fig. 16a. In general, the emission color of any phosphor can be represented by the (x , y) chromaticity co-ordinates (Sayed et al. 2011). The CIE co-ordinates are estimated using PL emission spectra and the values are listed in Table 4. It is noticed that the CIE co-ordinates of as-formed and calcined samples were located in the blue

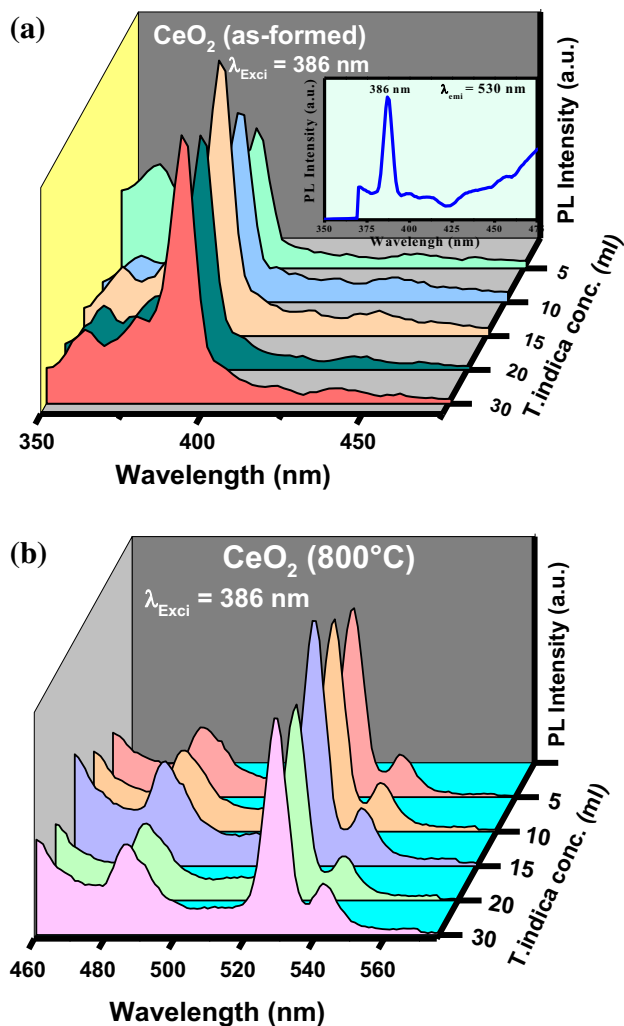


Fig. 15 PL emission spectra of **a** as-formed and **b** calcined CeO_2 NPs excited at 386 nm wavelength (Inset: excitation spectrum recorded at 530 nm emission)

region. The correlated color temperature (CCT) is one of the important parameters to know the color appearance of the light emitted by a source, relating it is color with respect to a reference light source when it is heated up to a specific temperature, in Kelvin (K) (Guo et al. 2012). The CCT is calculated and shown in Fig. 16b by the method as reported earlier (Shrivastava et al. 2015). The obtained values are summarized in Table 4.

Photocatalytic studies are carried out using 150×75 mm batch reactor at room temperature. Methylene blue is used as dye for photo degradation of CeO_2 NPs as catalyst. The particle size of as-formed CeO_2 NPs prepared with *T. indica* fuel (15 ml) was very small (5.2 nm) compared to other concentrations of the fuel; due to this reason, CeO_2 NPs with 15 ml samples were considered for photocatalytic activity. When solution of CeO_2 NPs with

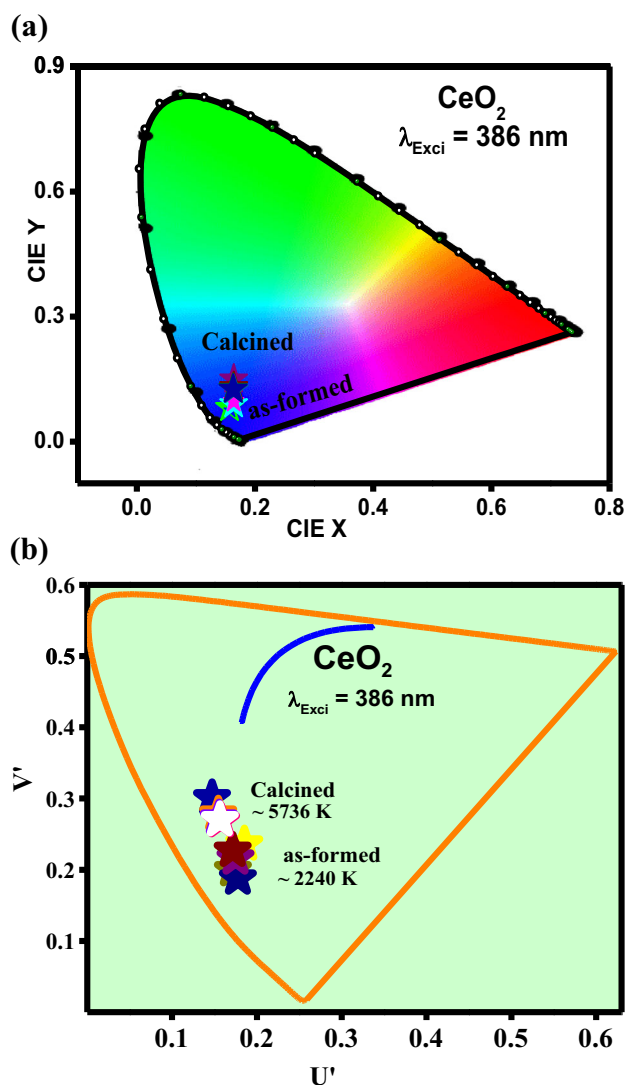
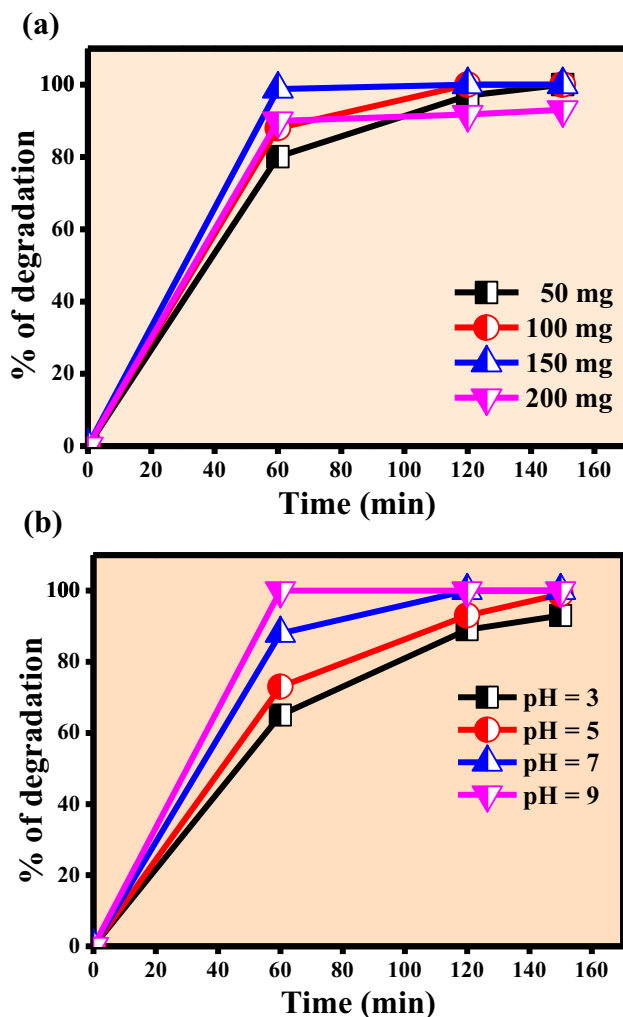


Fig. 16 **a** CIE and **b** CCT diagrams of as-formed and calcined CeO_2 (5–30 ml) NPs

dye was exposed to UV light, electron transfer from valence to conduction band by absorbing UV light. The e^- – h^+ pairs offers efficient path for oxidation and reduction reactions to degradation of MB dye. The generated electrons react with molecular oxygen and produce hydrogen-peroxide molecules in the aqueous medium and expressed by the following reactions. Conversely, the generated holes produce hydroxyl radicals from the water. These hydroxyl radicals act as an influential oxidizing agent to degradation of pollutant MB. The effect of pH concentration on the photocatalytic activity is also studied in detail. It is clear from the literature that photocatalytic activity depends on the pH value of solution. Here, four different pH concentrations effect on photocatalytic activity was studied. Surface property of CeO_2 and dislocation of dye molecule varies with the different pH value. In basic media, there is

Table 4 Photometric values of as-formed and calcined CeO₂ NPs

Sample	Fuel conc. (ml)	CIE		CCT		CCT (K)
		X	Y	U ¹	V ¹	
As-formed	5	0.1786	0.1011	0.1853	0.2360	2362
	10	0.1572	0.0812	0.1718	0.1998	2119
	15	0.1589	0.0747	0.1777	0.1880	1963
	20	0.1640	0.0901	0.1748	0.2161	2239
	30	0.1633	0.0966	0.1716	0.2270	2500
800 °C	5	0.1642	0.1491	0.1472	0.3009	7784
	10	0.1640	0.1640	0.1545	0.2780	5853
	15	0.1630	0.1630	0.1554	0.2722	5248
	20	0.1643	0.1643	0.1580	0.2687	4800
	30	0.1634	0.1634	0.1565	0.2701	4996

**Fig. 17** Effect of **a** catalytic load and **b** pH value on photocatalytic activity of calcined CeO₂ (15 ml) NPs

an increase in hydroxyl radicals which leads to the increase in photocatalytic activity (Arul et al. 2015; Khan et al. 2014; Lei et al. 2015).

Figure 17a shows the effect of catalytic load on the catalytic activity of CeO₂ NPs. To study the effect of catalytic load 5 ppm in 100 ml of water is maintained constant with varying catalytic load. The catalytic load increased up to 150 mg; the percentage of degradation was also increased and then remains constant for 200 mg catalytic load owing to the formation of turbidity in the solution which reduces the penetration of light through the solution. The following reactions explain the splitting of water molecule and dye degradation into organic acid and by-products.

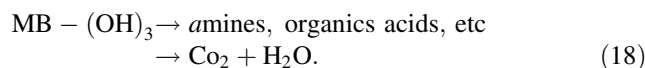
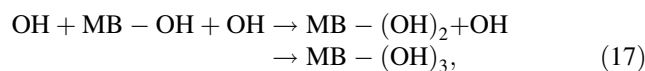
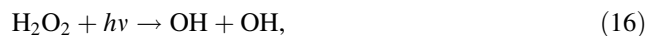
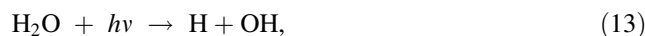
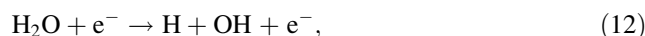
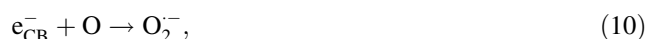


Figure 17b shows the effect of pH on catalytic activity of CeO₂ NPs. To study the effect of pH, 5 ppm dye

Fig. 18 Schematic representation to show the mechanism of photocatalytic degradation of MB using CeO₂ NPs

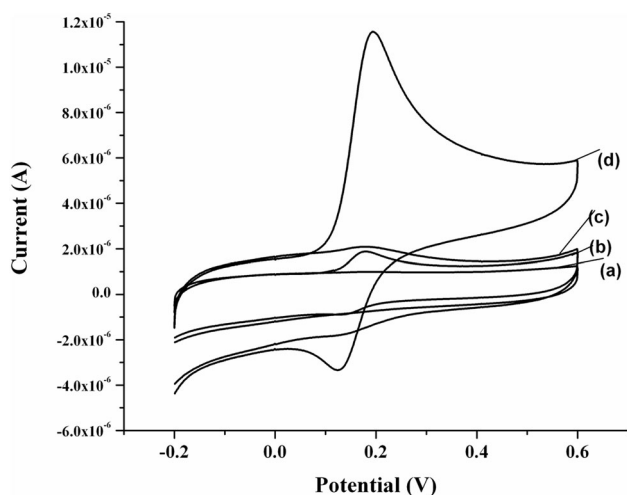
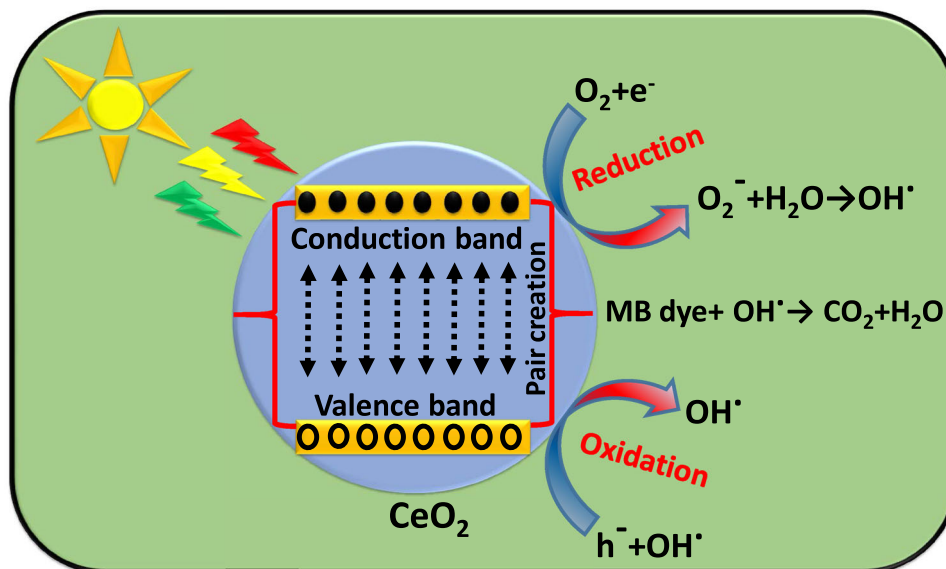


Fig. 19 CV plots of **a** bare carbon paste electrode in PBS buffer of pH = 7, **b** a + 0.5 mM dopamine, **c** calcined CeO₂ NPs modified carbon paste electrode in PBS buffer of pH 7, **d** c + 0.5 mM dopamine

concentration was maintained constant in 100 ml of water with 100 mg of catalytic load by varying pH concentrations. For pH 9, CeO₂ NPs have shown good photocatalytic activity while for pH 3 it exhibit poor activity which confirms that in basic medium activity it was more when compared with the acidic medium (Magesh et al. 2009; Wetchakun et al. 2012). Figure 18 shows the schematic representation of the mechanism involved in photocatalytic degradation of the MB dye using CeO₂ NPs as photocatalyst.

Figure 19 shows the cyclic voltograms (CVs) of as-formed CeO₂ NPs modified carbon paste electrode recorded in 0.5 mM dopamine concentration in PBS buffer of pH 7. The bare carbon paste electrode shows only a small

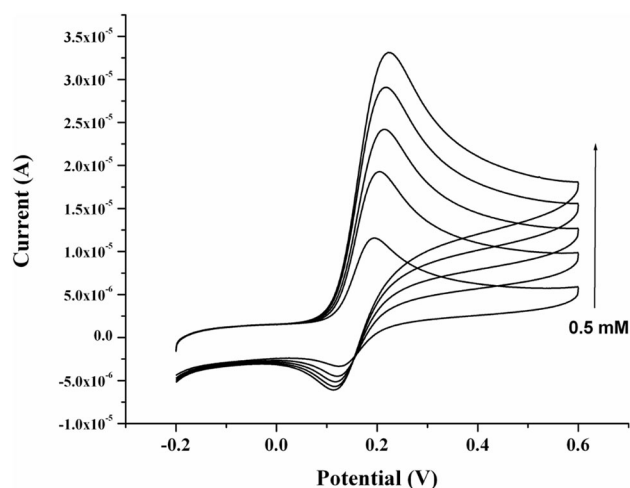


Fig. 20 CV plots of calcined CeO₂ NPs modified carbon paste electrode in PBS buffer of pH = 7 with dopamine concentrations ranging from 0.5 to 0.25 mM

oxidation peak centered at 0.2 V. Whereas, CeO₂ NPs modified carbon paste electrode shows well-defined oxidation peak at 0.2 V and also corresponding reduction peak around 0.13 V (Fig. 19c). These results confirm that presence of CeO₂ NPs on electrode assists in catalytic oxidation of dopamine. With increase in dopamine concentration, the anodic peak current also increases as shown in Fig. 20. This confirms that the redox peak corresponds to surface confined species (Li et al. 2015). The ratio of anodic and cathodic peak current was approximately equal to one, which indicates that the electrochemical reaction is highly reversible (Wei et al. 2006). The electrochemical sensing results obtained for modified electrodes CeO₂ NPs reveals the highly stable and can be used to fabricate good electrochemical sensing devices.

Conclusions

A simple green combustion route is used to prepare CeO₂ NPs using *T. indica* fruit extract as fuel. The structural, optical and catalytic properties of as-formed as well as calcined CeO₂ NPs are studied in detail. A cubic phase of prepared CeO₂ NPs is confirmed by PXRD patterns. The crystallite size, energy band gap and PL properties are highly dependent on concentration of fuel. The prepared CeO₂ NPs are highly porous and irregular shape with large number of surface voids. The particle size was estimated from TEM and found to be in the range of 5–40 nm which is in good agreement with PXRD results. From the CIE chromaticity diagrams, a blue color emission from the prepared sample is noticed. Further, modified electrodes by CeO₂ NPs exhibit enhanced electrochemical sensing properties and, hence, can be used to fabricate the electrochemical sensing devices. The CeO₂ NPs also showed good photocatalytic activity with respect to variation in pH and catalytic load. The above results clearly confirmed that the product obtained in green combustion route is quite useful for multifunctional applications.

Acknowledgements The author Dr. H Nagabhushana thanks VGST, Govt. of Karnataka, India [VGST/KFIST-4/GRD-489] for the sanction of this Project.

Open Access This article is distributed under the terms of the Creative Commons Attribution 4.0 International License (<http://creativecommons.org/licenses/by/4.0/>), which permits unrestricted use, distribution, and reproduction in any medium, provided you give appropriate credit to the original author(s) and the source, provide a link to the Creative Commons license, and indicate if changes were made.

References

- Arul NS, Mangalaraj D, Ramachandran R, Grace AN, Han JI (2015) Fabrication of CeO₂/Fe₂O₃ composite nanospindles for enhanced visible light driven photocatalysts and supercapacitor electrodes. *J Mater Chem A* 3:15248–15258
- Arumugam A, Karthikeyan C, Hameed ASH, Gopinath K, Gowri S, Karthika V (2015a) Synthesis of cerium oxide nanoparticles using *Gloriosa superba* L. leaf extract and their structural, optical and antibacterial properties. *Mater Sci Eng A* 49:408–415
- Arumugam A, Karthikeyan C, Haja Hameed AS, Gopinath K, Gowri S, Karthika V (2015b) Synthesis of cerium oxide nanoparticles using *Gloriosa superba* L. leaf extract and their structural, optical and antibacterial properties. *Mater Sci Eng C Mater Biol Appl* 49:408–415
- Arunkumar P, Ramaseshan R, Dash S, Basu J, Ravindran TR, Balakumar S, Suresh K (2014) Babu Texturing of pure and doped CeO₂ thin films by EBPVD through target engineering. *RSC Adv* 4:33338–33346
- Balakrishnan G, Raghavan CM, Ghosh C, Divakar R, Mohandas E, Song JI, Bae SI, Gyu Kim T (2013) X-ray diffraction, Raman and photoluminescence studies of nanocrystalline cerium oxide thin films. *Ceram Int* 39:8327–8333
- Basavaraj RB, Nagabhushana H, Darshan GP, Sharma SC, Venkatachalaiah K (2017) Ultrasound assisted rare earth doped Wollastonite nanopowders: labeling agent for imaging eccrine latent fingerprints and cheiloscopia applications. *J Ind Eng Chem* 51:90–105
- Binet C, Badri A, Lavalley J-C (1994) A spectroscopic characterization of the reduction of ceria from electronic transitions of intrinsic point defects. *J Phys Chem* 98:6392–6398
- Choi Y, Abernathy H, Chen HT, Lin M, Liu M (2006) Characterization of O₂-CeO₂ interactions using in situ Raman spectroscopy and first-principle calculations. *Chem Phys Chem* 7:1957–1963
- Dang F, Kato K, Imai H, Wada S, Haneda H, Kuwabara M (2010) Characteristics of CeO₂ nanocubes and related polyhedra prepared by using a liquid-liquid interface. *Cryst Growth Des* 10:4537–4541
- Darshan GP, Premkumar HB, Nagabhushana H, Sharma SC, DarukaPrasad B, Prashantha SC, Basavaraj RB (2016) Superstructures of doped yttrium aluminates for luminescent and advanced forensic investigations. *J Alloys Compd* 686:577–587
- Derakhshandeh PG, Soleimannejad J (2016) Sonochemical synthesis of a new nano-sized cerium (III) supramolecular compound. Precursor for nanoceria. *Ultrason Sonochem* 31:122–128
- Dhanalakshmi M, Nagabhushana H, Darshan GP, Basavaraj RB, Daruka Prasad B (2017) Sonochemically assisted hollow/solid BaTiO₃: Dy³⁺ microspheres and their applications in effective detection of latent fingerprints and lip prints. *J Sci Adv Mater Devices* 2:22–33
- Guo N, Zheng Y, Jia Y, Qiao H, You H (2012) Warm-white-emitting from Eu²⁺/Mn²⁺-Co doped Sr₃Lu(PO₄)₃ phosphor with tunable color tone and correlated color temperature. *J Phys Chem C* 116:1329–1334
- Huang P, Wu F, Zhu B, Gao X, Zhu H, Yan T, Huang W, Wu S, Song D (2005) CeO₂ nanorods and gold nanocrystals supported on CeO₂ nanorods as catalyst. *J Phys Chem B* 109:19169–19174
- Jamshidi P, Salavati-Niasari M, Ghanbari D, Shams HR (2013) Synthesis, characterization, photoluminescence and photocatalytic properties of CeO₂ nanoparticles by the sonochemical method. *J Cluster Sci* 24:1151–1162
- Jiang D, Zhang M, Li G, Jiang H (2012) Preparation and evaluation of MnOx-CeO₂ nanospheres via a green route. *Catal Commun* 17:59–63
- Jorge AB, Sakatani Y, Boissière C, Laberty-Roberts C, Sauthier G, Fraxedas J, Sanchez C, Fuertes A (2012) Nanocrystalline N-doped ceria porous thin films as efficient visible-active photocatalysts. *J Mater Chem* 22:3220–3226
- Ketzial JJ, Nesaraj AS (2011) Synthesis of CeO₂ nanoparticles by chemical precipitation and the effect of a surfactant on the distribution of particle sizes. *J Ceram Proc Res* 12:74–79
- Khan SB, Faisal M, Rahman MM, Akhtar K, Asiri AM, Khan A, Alamry KA (2013) Effect of particle size on the photocatalytic activity and sensing properties of CeO₂ nanoparticles. *Int J Electrochem Sci* 8:7284
- Khan MM, Ansari SA, Pradhan D, Han DH, Lee J, Cho MH (2014) Defect-induced band gap narrowed CeO₂ nanostructures for visible light activities. *Ind Eng Chem Res* 53:9754–9763
- Konysheva E, Francis S, Irvine J (2010) Crystal structure, oxygen nonstoichiometry, and conductivity of mixed ionic-electronic conducting perovskite composites with CeO₂. *J Electrochem Soc* 157:B159–B165
- Lee J, Park Y, Joo SW, Sohn Y (2014) Doping-concentration and annealing effects on photoluminescence profile of Eu(III)-doped CeO₂ nanorods. *Bull Korean Chem Soc* 35:3319

- Lehnen T, Schläfer J, Mathur S (2014) Rapid microwave synthesis of CeO₂ quantum dots. *Z Anorg Allg Chem* 640:819–825
- Lei W, Zhang T, Gu L, Liu P, Rodriguez JA, Liu G, Liu M (2015) Surface-structure sensitivity of CeO₂ nanocrystals in photocatalysis and enhancing the reactivity with nanogold. *ACS Catal* 5:4385–4393
- Li Z, Li L, Yuan Q, Feng W, Xu J, Sun L, Song W, Yan C (2008) Sustainable and facile route to nearly monodisperse spherical aggregates of CeO₂ nanocrystals with ionic liquids and their catalytic activities for CO oxidation. *J Phys Chem C* 112:18405–18411
- Li J, Lu G, Li H, Wang Y, Guo Y, Guo Y (2011) Facile synthesis of 3D flowerlike CeO₂ microspheres under mild condition with high catalytic performance for CO oxidation. *J Colloid Interface Sci* 360:93–99
- Li L, Wang S, Mu G, Yin X, Ou K, Yi L (2015a) A novel violet/blue light-emitting device based on Ce₂Si₂O₇. *Sci Rep* 5:16659. doi:10.1038/srep16659
- Li L, Wang H, Zou L, Wang X (2015b) Controllable synthesis, photocatalytic and electrocatalytic properties of CeO₂ nanocrystals. *RSC Adv* 5:41506–41512
- Li Z, Chen Y, Xin Y, Zhang Z (2015c) Sensitive electrochemical nonenzymatic glucose sensing based on anodized CuO nanowires on three-dimensional porous copper foam. *Sci Rep* 5:16115
- Lin Y, Wu Z, Wen J, Poepplmeier KR, Marks LD (2013) Imaging the atomic surface structures of CeO₂ nanoparticles. *Nano Lett* 14:191–196
- Liu IT, Hon MH, Teoh LG (2013) Structure and optical properties of CeO₂ nanoparticles synthesized by precipitation. *J Electron Mater* 42:2536–2541
- Lopez H, Mendoza H (2013) Temperature effects on the crystallization and coarsening of nano-CeO₂ powders. *ISRN Nano Mater* 2013:208614. doi:10.1155/2013/208614
- Lopez JM, Gilbank AL, Garcia T, Solsona B, Agouram S, Torrente-Murciano L (2015) The prevalence of surface oxygen vacancies over the mobility of bulk oxygen in nanostructured ceria for the total toluene oxidation. *Appl Catal B* 174:403–412
- Luo H, Bos AJ, Dobrowolska A, Dorenbos P (2015) Low-temperature VUV photoluminescence and thermoluminescence of UV excited afterglow phosphor Sr₃Al_xSi_{1-x}O₅: Ce³⁺, Ln³⁺ (Ln=Er, Nd, Sm, Dy and Tm). *Phys Chem Chem Phys* 17:15419–15427
- Maensiri S, Masingboon C, Laokul P, Jareonboon W, Promarak V, Anderson PL, Seraphin S (2007) Egg white synthesis and photoluminescence of platelike clusters of CeO₂ nanoparticles. *Cryst Growth Des* 7:950–955
- Maensiri S, Labuayai S, Laokul P, Klinkaewnarong J, Swatsitang E (2014) Structure and optical properties of CeO₂ nanoparticles prepared by using lemongrass plant extract solution. *Jpn J Appl Phys* 53:06JG14. doi:10.1088/0957-4484/16/9/006
- Magesh G, Viswanathan B, Viswanath R, Varadarajan T (2009) Photocatalytic behavior of CeO₂-TiO₂ system for the degradation of methylene blue. *Indian J Chem Sect A* 48:480
- Mallesappa J, Nagabhushana H, Sharma SC, Vidya YS, Anantharaju KS, Prashantha SC, DarukaPrasad B, RajaNaika H, Lingaraju K, Surendra B (2015) Leucas aspera mediated multifunctional CeO₂ nanoparticles: structural, photoluminescent, photocatalytic and antibacterial properties. *Spectrochim Acta Part A* 149:452–462
- Mallesappa J, Nagabhushana H, DarukaPrasad B, Sharma BS, Vidya YS, Anantharaju KS (2016) Structural, photoluminescence and thermoluminescence properties of CeO₂ nanoparticles. *Opt Int J Light Electron Opt* 127:855–861
- Mallesappaa J, Nagabhushanab H, Sharmac SC, Sunithab DV, Dhnananjayad N, Shivakumarae C, Nagabhushana BM (2014) Self propagating combustion synthesis and luminescent properties of nanocrystalline CeO₂: Tb³⁺ (1–10 mol%) phosphors. *J Alloys Compd* 590:131–139
- Morshed A, Moussa M, Bedair S, Leonard R, Liu S, El-Masry N (1997) Violet/blue emission from epitaxial cerium oxide films on silicon substrates. *Appl Phys Lett* 70:1647–1649
- Periyat P, Laffir F, Tofail S, Magner E (2011) A facile aqueous sol-gel method for high surface area nanocrystalline CeO₂. *RSC Adv* 1:1794–1798
- Sahu HR, Rao GR (2000) Characterization of combustion synthesized zirconia powder by UV-vis, IR and other techniques. *Bull Mater Sci* 23:349–354
- Saif M, Shebl M, Nabeel A, Shokry R, Hafez H, Mbarek A, Damak K, Maalej R, Abdel-Mottaleb M (2015) Novel non-toxic and red luminescent sensor based on Eu³⁺: Y₂Ti₂O₇/SiO₂ nano-powder for latent fingerprint detection. *Sens Actuators B* 220:162–170
- Sathyamurthy S, Leonard KJ, Dabestani RT, Paranthaman MP (2005) Reverse micellar synthesis of cerium oxide nanoparticles. *Nanotechnology* 16:1960. doi:10.1088/0957-4484/16/9/089
- Sayed FN, Grover V, Dubey KA, Sudarsan V, Tyagi AK (2011) Solid state white light emitting systems based on CeF₃: RE³⁺ nanoparticles and their composites with polymers. *J Colloid Interface Sci* 353:445–453
- Sharma V, Das A, Kumar V, Ntwaeaborwa O, Swart H (2014) Potential of Sr₄Al₁₄O₂₅: Eu²⁺, Dy³⁺ inorganic oxide-based nanophosphor in Latent fingerprint detection. *J Mater Sci* 49:2225–2234
- Shivaram M, Nagabhushana H, Sharma SC, Prashantha SC, DarukaPrasad B, Dhnananjaya N, HariKrishna R, Nagabhushana BM, Shivakumara C, Chakradhar RPS (2014) Synthesis and luminescence properties of Sm³⁺ doped CaTiO₃ nanophosphor for application in white LED under NUV excitation. *Spectrochim Acta Part A* 128:891–901
- Shrivastava R, Kaur J, Dash M (2015) Studies on white light emission of Sr₂MgSi₂O₇ doped with Dy³⁺ phosphors. *Superlattices Microstruct* 82:262–268
- Sun C, Li H, Zhang H, Wang Z, Chen L (2005) Controlled synthesis of CeO₂ nanorods by a solvothermal method. *Nanotechnology* 16:1454. doi:10.1088/0957-4484/16/9/006
- Suresh C, Nagabhushana H, Darshan GP, Basavaraj RB, DarukaPrasad B, Sharma SC, Sateesh MK, ShabaaBegum JP (2017) Lanthanum oxyfluoride nanostructures prepared by modified sonochemical method and their use in the fields of optoelectronics and biotechnology. *Arabian J Chem*. doi:10.1016/j.arabj.2017.03.006
- Venkatachalaiah K, Nagabhushana H, Darshan GP, Basavaraj RB, DarukaPrasad B (2017) Novel and highly efficient red luminescent sensor based SiO₂@ Y₂O₃: Eu³⁺, M⁺ (M⁺= Li, Na, K) composite core-shell fluorescent markers for latent fingerprint recognition, security ink and solid state lightning applications. *Sens Actuators B* 251:310–325
- Wang G, Mu Q, Chen T, Wang Y (2010) Synthesis, characterization and photoluminescence of CeO₂ nanoparticles by a facile method at room temperature. *J Alloys Compd* 493:202–207
- Wang M, Li M, Yang M, Zhang X, Yu A, Zhu Y, Qiu P, Mao C (2015a) NIR-induced highly sensitive detection of latent fingerprints by NaYF₄: Yb, Er upconversion nanoparticles in a dry powder state. *Nano Res* 8:1800–1810
- Wang M, Li M, Yu A, Wu J, Mao C (2015b) Rare earth fluorescent nanomaterials for enhanced development of latent fingerprints. *ACS Appl Mater Interfaces* 7:28110–28115
- Wang M, Zhu Y, Mao C (2015c) Synthesis of NIR-Responsive NaYF₄: Yb, Er upconversion fluorescent nanoparticles using an optimized solvothermal method and their applications in enhanced development of latent fingerprints on various smooth substrates. *Langmuir* 31:7084–7090

- Weber M (1973) Optical spectra of Ce^{3+} and Ce^{3+} sensitized fluorescence in $YAlO_3$. *J Appl Phys* 44:3205–3208
- Wei Y, Li M, Jiao S, Huang Q, Wang G, Fang B (2006) Fabrication of CeO_2 nanoparticles modified glassy carbon electrode and its application for electrochemical determination of UA and AA simultaneously. *Electrochim Acta* 52:766–772
- Wetchakun N, Chaiwichain S, Inceesungvorn B, Pingmuang K, Phanichphant S, Minett AI, Chen J (2012) $BiVO_4/CeO_2$ nanocomposites with high visible-light-induced photocatalytic activity. *ACS Appl Mater Interfaces* 4:3718–3723
- Xiaoyuan J, Guanglie L, Renxian Z, Jianxin M, Yu C, Xiaoming Z (2001) Studies of pore structure, temperature-programmed reduction performance, and micro-structure of CuO/CeO_2 catalysts. *Appl Surf Sci* 173:208–220
- Xu B, Zhang Q, Yuan S, Liu S, Zhang M, Ohno T (2017) Synthesis and photocatalytic performance of yttrium-doped CeO_2 with a hollow sphere structure. *Catal Today* 281:135–143
- Yan B, Zhu H (2008) Controlled synthesis of CeO_2 nanoparticles using novel amphiphilic cerium complex precursors. *J Nanopart Res* 10:1279–1285
- Yuan B, Long Y, Wu L, Liang K, Wen H, Luo S, Huo H, Yang H, Ma J (2016) $TiO_2@h-CeO_2$: a composite yolk-shell microsphere with enhanced photodegradation activity. *Catal Sci Technol* 6:421–428
- Zhou Y, Rahaman MN (1997) Effect of redox reaction on the sintering behavior of cerium oxide. *Acta Mater* 45:3635–3639

Publisher's Note

Springer Nature remains neutral with regard to jurisdictional claims in published maps and institutional affiliations